

# Complexity parameters of solar-wind magnetic fluctuations at 1 AU during SC23 and SC24

B. Acosta-Tripailao<sup>1</sup>, Denisse Pastén<sup>1</sup>, and Pablo S. Moya<sup>1</sup>

Departamento de Física, Facultad de Ciencias, Universidad de Chile, Las Palmeras 3425, Ñuñoa, Santiago, Chile  
e-mail: bacostaazocar@gmail.com; denisse.pasten.g@gmail.com; pablo.moya@uchile.cl

Received 21 October 2022 / Accepted 18 January 2023

## ABSTRACT

**Context.** The solar wind develops a highly turbulent character during its expansion, where plasma and electromagnetic fluctuations coexist. Considering the presence of turbulence in the plasma as a complex system, the turbulence in the solar wind in general has been measured and studied using different techniques from a systems science point of view. These techniques provide the opportunity to obtain preliminary information even before much of the physics can be assimilated and integrated.

**Aims.** We describe this plasma as a complex system in order to understand solar wind dynamics from a new perspective. Several missions provide a wide range of data concerning critical astrophysical phenomena. This poses a challenge to implement new effective methods to complement the characterization of the constantly new, and sometimes highly reduced information, especially when dealing with observational data with intermittent gaps.

**Methods.** We work with magnetic fluctuation time series data obtained from the Wind mission at 1 AU in order to characterize the fast and slow solar wind behavior during solar cycles 23 (SC23) and 24 (SC24). We applied the horizontal visibility graph (HVG) method to obtain the evolution of measurements of Kullback-Leibler divergence (KLD),  $D$ , and the characteristic exponent,  $\gamma$ , over time. Both are complexity parameters extracted from the degree distributions of the networks.

**Results.** By contrasting our complexity parameters,  $\gamma$  and  $D$ , with solar activity characterized by the number of sunspots and solar wind speed, we obtain significant intercorrelations among them during both cycles and ascending, descending, minimum, and maximum phases. According to  $\gamma$  values, the magnetic fluctuations of the solar wind are a correlated stochastic time series at 1 AU. Also, the divergence  $D$  recognizes SC23 as the most dissipative and identifies the slow wind as more variable than the fast wind, with a better anti-correlation in the minima phases. This study reveals that in terms of solar phases  $\gamma_{\min} > \gamma_{\text{des}} > \gamma_{\text{asc}} > \gamma_{\max}$ , and  $D_{\min} < D_{\text{des}} < D_{\text{asc}} < D_{\max}$ . We show that the HVG technique leads to results that are consistent with the complex nature of solar wind turbulence.

**Key words.** magnetic fields – plasmas – turbulence – methods: statistical – Sun: activity – solar wind

## 1. Introduction

Studies have revealed the existence of several different dynamics in the solar wind depending on its origin and the distance to the Sun. To discriminate and classify solar wind type between slow and fast, we can consider five relevant parameters, namely radial velocity, proton density, proton temperature, the oxygen ion ratio, and the magnetic compressibility factor (Wawrzaszek et al. 2019). These relevant parameters reflect the dynamics of the solar wind while it expands from the continuation of the solar corona until coming into contact and interacting with the Earth's magnetosphere. In this path, this plasma reaches velocities of approximately  $250\text{--}800\text{ km s}^{-1}$ . At the same time, it is subject to the solar activity cycle of approximately 11 yr and the solar magnetic cycle of approximately 22 yr (the Hale cycle; Balogh & Lanzerotti 2008). The solar wind develops a highly turbulent character during its expansion (Bruno & Carbone 2013). Wherever we observe the solar wind, many nonlinear phenomena are involved at many scales.

Many studies have used different measurement techniques from the field of systems science to investigate turbulence in the solar wind. Wawrzaszek et al. (2019) studied the intermittency of the magnetic field turbulence in the solar wind using data obtained by the Ulysses spacecraft. These authors developed

comprehensive data-selection criteria to discriminate between the state of the slow and fast solar wind without simply relying on the velocity parameter. They reported a slight decrease in the multifractality (intermittency) of the solar wind plasma with radial distance. Wawrzaszek et al. (2019) interpreted this radial dependence as being due to a slower evolution of the turbulence beyond the ecliptic plane and to the lower efficiency of the intermittency drivers with distance from the Sun. These authors also explained the change in wind type during the solar cycle as being related to a new type of slow Alfvénic solar wind. Furthermore, Wawrzaszek et al. (2019) observed that the slow solar wind at the maximum of solar cycle 23 exhibits a lower level of multifractality than the fast solar wind.

The occurrence of intermittency in plasma turbulence has been explored by studying the deviation of the probability distribution function (PDF) for both velocity and magnetic fluctuations from the Gaussian distribution (Marsch & Tu 1994; Sorriso-Valvo et al. 1999, 2001). Some studies show a strong relationship between intermittency fluctuations and multifractal behavior resulting from the solar wind turbulent cascade Sorriso-Valvo et al. 2017. In other studies, kinetic-scale fluctuations reveal monofractal behavior (Alberti et al. 2019; Roberts et al. 2020; Chhiber et al. 2021), as opposed to multifractality.

The Lyapunov exponent has been widely used to analyze the dynamics of space plasmas. Gupta et al. (2008) and Redaelli & Macek (2001) studied the Lyapunov exponent of velocity fluctuations measured by the Helios spacecraft. Gupta et al. (2008) analyzed the time series of the solar wind speed fluctuations to understand the local dynamics of the slow wind speed fluctuations. The authors analyzed the Lyapunov exponents and suggested that there are inherent changes in the dynamics throughout solar cycle 21 and that there is low-dimensional chaotic behavior in the underlying dynamics. Macek & Redaelli (2001), Redaelli & Macek (2001) analyzed the fluctuations of the low-speed stream of the solar wind using a nonlinear filter to approximate the nonlinear behavior of the flow and also obtained more reliable estimates of the Lyapunov exponent and the Kolmogorov entropy. These authors found that the solar wind in the inner heliosphere is probably a deterministic chaotic system.

Continuing with natural complexity measures to detect dynamic changes in time series, Suyal et al. (2012) calculated the permutation entropy of the solar wind time series at different phases of solar activity cycle 23. These authors worked with measurements obtained by the ACE spacecraft, and observed that the complexity of the solar wind velocity fluctuations at 1 AU is dominated by the hysteresis phenomenon when following the ascending and descending phases of the solar cycle. This situation led them to suggest the presence of multistability in the dynamics governing the solar wind speed throughout a solar activity cycle. Then, Suyal et al. (2014) estimated the Kullback–Leibler divergence (KLD) of the solar wind velocity via complex networks. These authors analyzed solar wind speed measurements obtained by the ACE and Helios spacecraft and calculated the KLD at different phases of the solar activity cycles 21 and 23, concluding that the solar wind speed is more variable during the maximum and minimum activity phases. At the same time, Suyal et al. (2014) found that solar wind speed is less variable during the ascending and descending phases of the solar activity cycle. Moreover, they also concluded that the irreversibility parameter (KLD) over a solar activity cycle is similar at both 0.3 AU and 1 AU.

These studies suggest that the solar wind turbulence is of a nonuniversal and complex nature. Complex networks are often used to describe the origin of the complexity in complex systems. Systems science analysis can be applied even before much of the physics is identified or understood (Borovsky 2021). A variety of missions are providing a wide range of data that it is hoped will help us to understand relevant astrophysics phenomena. This poses a challenge to implement new effective methods to complement the characterization of the constantly new, and sometimes highly reduced information. To study solar-wind fluctuations, rely on complex network tools, including a family of visibility algorithms (Lacasa et al. 2008, 2009). These tools can be used to convert time series into graphs, where the structure of the series in terms of its temporal ordering and data magnitude is preserved in the topology of the graph. This procedure builds a natural bridge between complex network theory and time-series analysis. The horizontal visibility graph (HVG; Lacasa et al. 2012) method allows us to obtain complexity parameters with which to analyze time series of solar wind data, such as relative entropy and the nature of the time correlations of the system. The HVG method helps us to avoid the tedium and high computational cost entailed by other commonly used methods. The visibility algorithm has been used before in plasma physics, space plasmas, and astrophysics, among others (Suyal et al. 2014; Acosta-Tripailao et al. 2019, 2021, 2022; Mohammadi et al. 2021).

Here we present a novel study describing and analyzing magnetic field data via complex networks built using the HVG method. The HVG can schematically extract the intrinsic information present in the data by considering its temporal occurrence and magnitude. Specifically, we apply the HVG technique to data obtained by the Wind spacecraft, which takes in situ measurements of solar wind magnetic fluctuations at 1 AU. With this method, we calculate the  $\gamma$ -exponent, a measure representing the nature of the correlations dominating the time series; and the KLD or relative entropy, a measure of the degree of time irreversibility in the time series. We use these to explore the dissipative characteristics of solar-wind dynamics closer to the Earth throughout solar cycles 23 and 24. Moreover, we compare these complexity parameters in order to distinguish between the type of solar wind (fast or slow).

This article is organized as follows. Section 2 is dedicated to developing a complete description of the HVG method, defining how we obtain the critical exponent and the KLD from the complex network, the limit between correlated stochastic and chaotic time series, which is related to the critical exponent, and the calculation of the reversibility range, which is related to the KLD. Section 3 provides a summary of the significant features of observations and characteristics of solar phases along SC23 and SC24. We present our results in Sect. 4 after applying the HVG method on magnetic time series, and we finally discuss our findings and provide a summary of our conclusions in Sect. 5.

## 2. Description of the horizontal visibility graph

With this study we aim to interweave the key aspects driving the topology of complex networks with the physical mechanisms responsible for the variability of solar wind magnetic fluctuations. We therefore proceed to study the topology of the interactions among the components of a time series, that is the connections among nodes within a data set that evolves over time. Tools and measures need to be applied to quantitatively assess the principles that organize the information of a given system (Albert & Barabási 2002). In this context, the tools of complex networks offer a different approach to describe the non-trivial interconnected information presented in a time series. With the HVG algorithm, these connections are related to the variability and the succession of events over time.

A time series  $\{x_i\}_{i=1,\dots,n}$  has  $n$  data. The algorithm builds a network where each data point in the series is a node. For complex networks, we connect the nodes following the geometrical criterion of horizontal visibility. Then, for outgoing connections,  $i$  is a node that will always be connected with its consecutive node  $i + 1$ , and will be connected to other future nodes  $j$  if

$$x_i, x_j > x_m \quad \forall m : i < m < j, \text{ with } j > i + 1, \quad (1)$$

and this is fulfilled within the time series (Luque et al. 2009). Now in reverse order, for ingoing connections,  $i$  is a node that will always be connected with its previous node  $i - 1$ , and will be connected to other past nodes  $j$  if

$$x_i, x_j > x_m \quad \forall m : i > m > j, \text{ with } j < i - 1. \quad (2)$$

Once all the links are established for the  $i$  node, each node will have degrees denoted  $k_{\text{out}}$  and  $k_{\text{in}}$  for outgoing and ingoing connections, respectively, based on the number of times the condition (1) is satisfied in the time direction, and (2) in the inverse time direction. The presence of a data magnitude greater than or equal to the data under study interrupts its visibility. With these

two types of directed connections, we can assign to each node the undirected degree  $k$  as the sum of both:  $k = k_{\text{in}} + k_{\text{out}}$ .

To characterize the information extracted from the original time series, we seek to know how these nodes are distributed, that is, their probability of degree distribution. In order to analyze the dynamics between nodes, degree distributions have a crucial role to play and provide valuable statistical information. The degree distributions of a network describe the probability with which a node has a given degree.

For undirected links, the degree distribution will be  $P(k) = n_k/n$ , where  $n_k$  is the number of occurrences of degree  $k$  among the  $n$  total nodes. The degree distribution for undirected degrees has an exponential behavior of the form  $P(k) = \frac{1}{3} \left(\frac{2}{3}\right)^{k-2}$  (Luque et al. 2009), which can be rewritten as

$$P(k) \sim \exp(-\gamma_{\text{un}}k), \quad (3)$$

where  $\gamma_{\text{un}} = \ln(3/2) \approx 0.405$ , which is a limit for the uncorrelated situation proposed by Lacasa & Toral (2010) to distinguish between correlated stochastic ( $\gamma > \gamma_{\text{un}}$ ) and chaotic ( $\gamma < \gamma_{\text{un}}$ ) time series. Hence, the idea is to obtain the degree distributions and linearly fit  $\log P(k) = -\gamma k$  to obtain the parameter  $\gamma$  and compare around the limit value  $\gamma_{\text{un}}$ .

For directed links, we have degree distributions  $P_{\text{in}} = P(k_{\text{in}}) = n_{\text{in}}/n$  and  $P_{\text{out}} = P(k_{\text{out}}) = n_{\text{out}}/n$ , where  $n_{\text{in}}$  and  $n_{\text{out}}$  are the number of occurrences of degrees  $k_{\text{in}}$  and  $k_{\text{out}}$ , respectively. From a physical perspective, the irreversibility trace is related to the production of a macroscopic amount of entropy in the system due to a dissipative work. Our aim is to evaluate the irreversibility of the physics captured by the time series, and how different the succession between past and future events is. For this particular purpose, a measure that precisely distinguishes between two degree distributions is the KLD or relative entropy.

The KLD is a statistical measure of “distinguishability” (Lacasa et al. 2012) introduced from information theory to quantify the degree of temporal irreversibility. Moreover, this irreversibility implies a lower bound on the entropy production of the process that generates the time series. Roldán & Parrondo (2012) showed that the KLD is a powerful tool for detecting nonequilibrium states and for evaluating the entropy production of a process, at least as an estimator. The KLD between the two probability functions is defined as (Cover & Thomas 2006)

$$D[P_{\text{out}}(k)||P_{\text{in}}(k)] = \sum_k P_{\text{out}}(k) \log \frac{P_{\text{out}}(k)}{P_{\text{in}}(k)}; \quad (4)$$

it is the weighted average of the logarithmic difference between the  $P_{\text{out}}$  and  $P_{\text{in}}$  probabilities, where the average is taken using the  $P_{\text{out}}$  probabilities. For logarithm base  $e$ , the divergence is expressed with the natural unit of information. KLD is always positive by definition and is zero if and only if  $P_{\text{in}} = P_{\text{out}}$ . In addition, there are cases where for some  $k$  degree, no node has presented  $k$  ingoing connections but does have outgoing connections. This description implies  $P_{\text{out}}(k) > 0$  and  $P_{\text{in}}(k) = 0$ . As the KLD is a weighted average between differences, we consider each of these cases as a null contribution instead of infinity, because there is no probability to compare. This last assumption sometimes generates negative values in  $D$ ; if this occurs, we define the case as an outlier and discard it.

### 3. Solar wind and solar cycles

The intercorrelation between solar activity and solar wind is a topic of fundamental importance. The global structure of

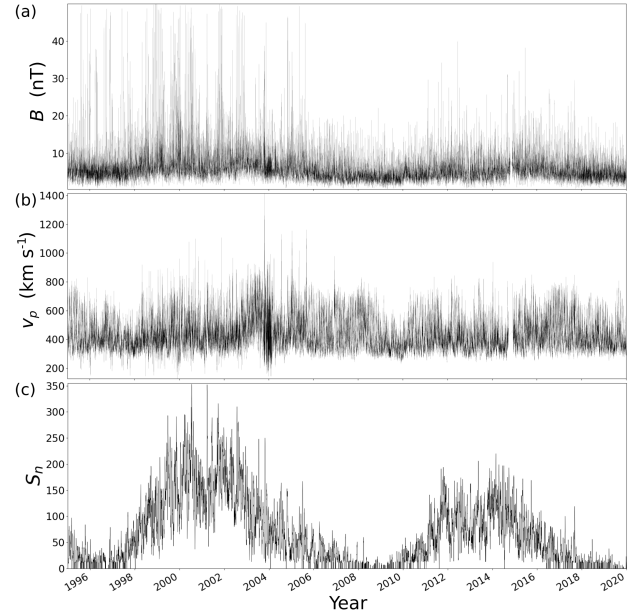


**Fig. 1.** Time series of the data used in this study. This data set is composed of (a) solar wind magnetic field,  $B$ , as input for the method HVG, (b) solar wind proton bulk speed,  $v_p$ , and (c) sunspot number,  $S_n$ , as variables for comparison. The first two data sets were obtained from NASA CDAweb by Wind Mission, while the last data set was obtained from World Data Center SILSO by the Royal Observatory of Belgium. The data shown correspond to measurements taken from 1 Jan. 1995 to 31 Dec. 2019, covering solar cycles 23 and 24.  $B$ ,  $v_p$ ,  $S_n$  time resolutions are 1 h, 92 s, and 1 day, respectively.

the three-dimensional solar wind at solar maximum is entirely different than at solar minimum (McComas et al. 2003). The sunspot number is a synthetic index that quantifies the solar variability due to magnetic activity (Reda et al. 2021). Thus, the sunspot number  $S_n$  is a direct indicator of solar activity because smoothed sunspot numbers have characterized its cyclic variations as the first proxy for solar phases (Shepherd et al. 2014). The Sun’s magnetic activity increases with solar activity, which can be visualized in four phases: minimum, ascending, maximum, and descending (Kilpua et al. 2015; Reyes et al. 2021). In particular, the solar minimum is a period of low magnetic activity on the Sun between the descending phase of the old cycle and the ascending phase of the new cycle. This transition is marked by the reversal of the magnetic activity gradient, a phase in which the Sun’s magnetic field is completely reversed.

Of the two cycles studied here, SC24 exhibited the lowest activity. The previous five cycles had been notably productive in terms of sunspots, but SC24 was not. The minimum phase transition between SC23 and SC24 took longer than usual (7 Jan. 2007 to 31 Oct. 2009) and reached the lowest level in about a century, specifically since 1913. This situation can be understood as being due to the slight decrease in the activity of SC23 and the slight increase in SC24. This decrease in the Sun’s activity was also manifested in the solar magnetic field variations (de Toma et al. 2010), as the interplanetary magnetic field showed significantly lower values during the years of the minimum. The observations made in the near-Earth ecliptic plane were, surprisingly, the lowest in the in situ solar wind magnetic measurements from 1963 until then according to the OMNI database compilation. Therefore, this cycle change, a novelty of the last ~50 yr of Sun observation, offers a unique opportunity to base our study on the comparative search for intercorrelations

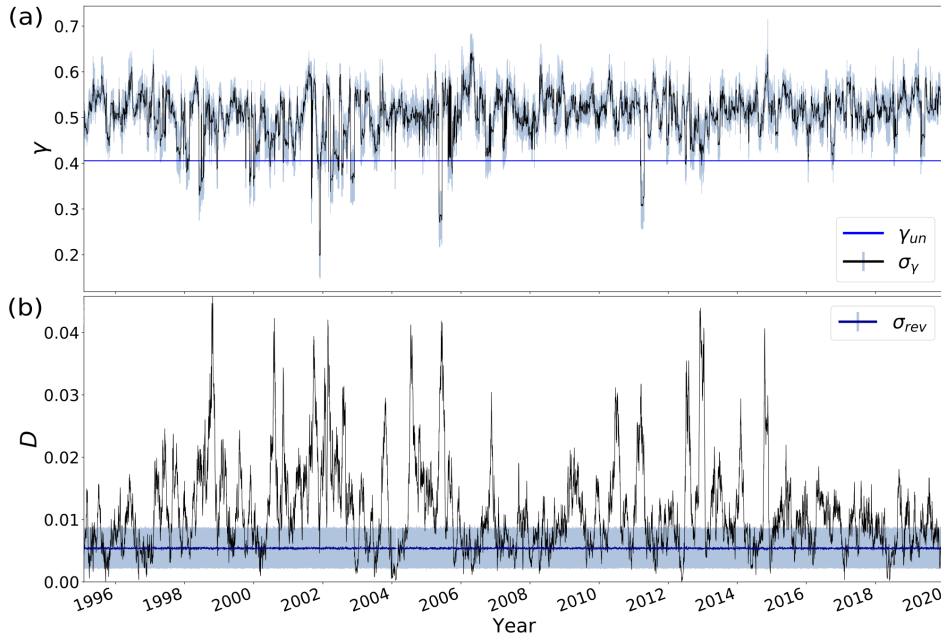


**Fig. 2.** Temporal evolution of the (a)  $\gamma$  and (b)  $D$  of the magnetic field from 31 Jan. 1995 to 2 Dec. 2019, considering a moving window that covers two months with a one-day resolution (black solid curves). (a) In the *top panel*, light blue is used to indicate the  $\gamma$  error,  $\sigma_\gamma$ , obtained from the linear fit of  $\log(P(k))$ . (b) In the *bottom panel*, light blue is used to indicate the reversibility range. The reversibility range results from the application of the HVG algorithm to randomly disordered copies of the data in every window, obtaining the standard deviation  $\sigma_{\text{rev}}$  around the average divergence (in dark blue) computed using the disordered data.

with the complexity parameters. With this background, we can judge the sensitivity of the method.

Regarding the solar activity–solar wind relation, Podesta et al. (2007) found a measurable difference between the power-law exponents of the velocity and magnetic field fluctuations (values near  $-3/2$  and  $-5/3$ , respectively). These authors based their analysis on four different time intervals of solar wind plasma and magnetic field data obtained by the Wind spacecraft near the end of solar cycle 22 and at other times throughout solar cycle 23 in the ecliptic plane near 1 AU. Furthermore, they indicated that this difference between the power law exponents persists throughout the solar cycle. However, Roberts (2007) concluded that the discrepancy between the magnetic field spectral power law and velocity spectral power law exponents is only temporary and corresponds to the phase of evolution in the spectra towards turbulence.

The dissipative processes in the solar wind are related to the magnitude and direction of the magnetic field, which influence the determination of the Reynolds number as an indicator of turbulence (Bruno & Carbone 2013). As space environments usually correspond to poorly collisional turbulent plasmas, understanding how energy is transmitted and dissipated is a complex task in space plasma physics. In these environments, very few Coulomb collisions occur, and therefore the plasma particles interact mostly through electromagnetic forces whose range is determined by the Debye length. It is stipulated that energy dissipation in the solar wind occurs to a greater extent at small scales where wave–particle interactions should be efficient (Bruno & Carbone 2013). However, in a turbulent system, all dynamically interesting scales are excited, that is, the energy is distributed over all scales through the energy cascades associated with the turbulence itself. Under this context, the increments of the magnetic field strength provide information that can be used to search for and study coherent structures at different scales (Greco et al. 2017). Here, we address this question by analyzing the variability of the magnetic field magnitude, which helps to understand turbulence phenomenology and dissipative processes via a complex network approach.

We work with magnetic field and proton bulk speed data measured by the Magnetic Field Investigation (MFI;

Lepping et al. 1995) and the Solar Wind Experiment (SWE; Ogilvie et al. 1995) instruments on board the Wind spacecraft (obtained from NASA CDAweb); and with sunspot number data obtained from World Data Center SILSO. We use one-hour cadence Wind-MFI data measured at 1 AU on the ecliptic plane. The data set corresponds to measurements taken from 1 Jan. 1995 to 31 Dec. 2019, which includes the end of SC22, and completely covers cycles 23 and 24 and the beginning of SC25. We focus on SC23 and SC24. SC23 dates from 6 May 1996 to 23 Nov. 2008. SC24 dates from 24 Nov. 2008 to 24 Nov. 2019. The cycle and phase start and end dates are specified by Reyes et al. (2021). Figure 1 displays the time series of the data set used in this study. Figure 1a shows the solar wind magnetic field as input for the method HVG. Figure 1b shows the proton bulk speed with a 92-s cadence. Figure 1c shows the daily sunspot number. In our analysis, the latter two are used to compare solar wind behavior and solar activity.

## 4. Results

This study modeled the time series of magnetic fluctuations data collected from the Wind satellite observations as HVGs over time. For this purpose, moving windows in time were used, covering approximately two months of magnetic data (1440 data points, or nodes, covered by each network), with an overlap of approximately one day (the distance between consecutive data windows is 24 data points, or nodes). The moving windows begin on 1 Jan. 1995, and when the series cannot contain the same amount of two-month data towards the end of the series, the calculation is stopped. Each of these windows encapsulates the data. In that way, we map the information into a network under the geometrical criterion of horizontal visibility. Thus, through this mapping, we built every complex network with the same number of nodes and assigned the mean of the time interval covered by the moving window. Every network has one degree distribution  $P$  from undirected HVG, and two degree distributions  $P_{\text{in}}$  and  $P_{\text{out}}$  from directed HVG, as explained in Sect. 2. From these, we calculated the  $\gamma$  and  $D$  values in time using data shown by Fig. 1a. Following the outliers criterion mentioned in Sect. 2, the case of negative values when computing the KLD

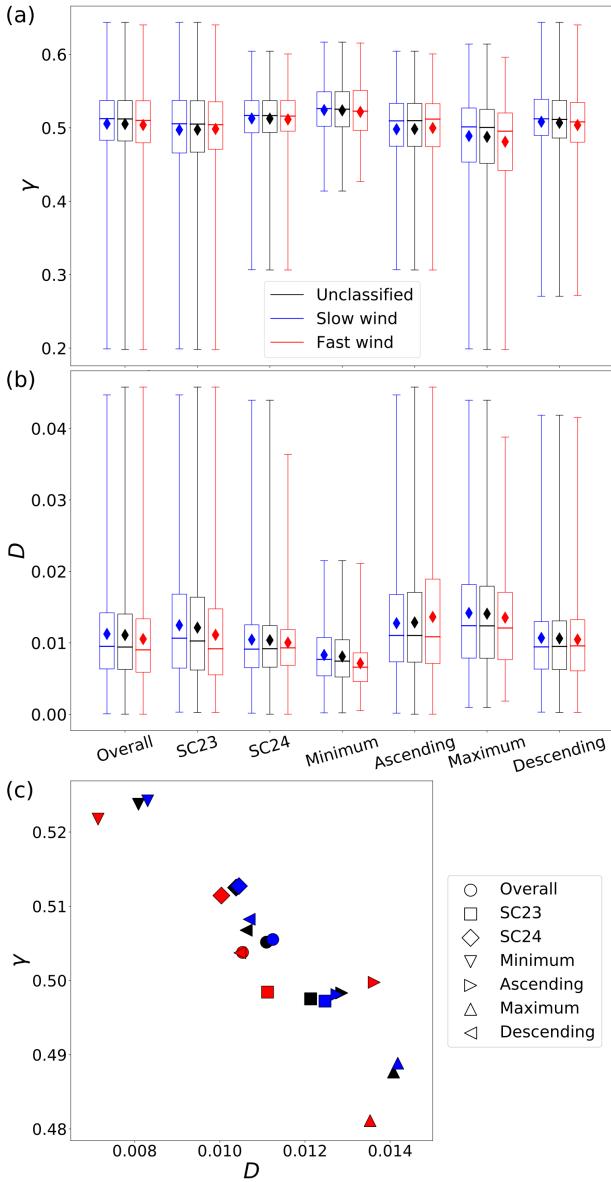


**Fig. 3.** Solar wind: boxplot diagrams in the *first two panels* show the mean (diamond symbol), median (horizontal line), and 25%–75% percentiles of (a)  $\gamma$  and (b)  $D$  values for overall data by cycle, and by total cycle-independent phases, according to the following classification: slow and fast for speeds under and over  $500 \text{ km s}^{-1}$ , respectively. The whisker indicates the range between minimum and maximum values calculated. (c) Scatter plot between the mean values of  $\gamma$  and  $D$  for solar wind without classifying (black), slow wind (blue), and fast wind (red).

occurred in only 4% of the results (39 of 8959 moving windows) and these were discarded. Figure 2 contains the temporal evolution of  $\gamma$  and  $D$  for the magnetic field time series. In addition, the limit  $\gamma_{\text{un}} \approx 0.405$  between correlated stochastic and chaotic time series is mentioned in Fig. 2a (Lacasa & Toral 2010), and the error in  $\gamma$  and  $\sigma_\gamma$  was calculated from the exponential fit. Also, in Fig. 2b, to determine a range of reversibility, we applied the HVG algorithm to 1000 randomly disordered copies of the data in every moving window, obtaining the standard deviation  $\sigma_{\text{rev}}$  around the mean divergence computed using the disordered data, also with an overlap of 24 h.  $\gamma$  is almost always above the limit, and  $D$  goes in and out of the reversibility range.

The information in Fig. 3 allows us to infer a statistical analysis of our results relative to the behavior of the solar wind

through the solar cycles. Figures 3a–b present information for unclassified solar wind (i.e., fast and slow solar winds combined). On average and in terms of cycles, the  $D$  divergence was higher for SC23, and the  $\gamma$  exponent was higher for SC24. In contrast to the overall behavior, the  $D$  measure appears to vary as a function of phase. However, the  $\gamma$  value does not vary considerably, as all values within the central quartiles are concentrated around  $\gamma = 0.5 > \gamma_{\text{un}}$ . Therefore, we conclude these are predominantly correlated stochastic and not uncorrelated chaotic time series. When  $\gamma$  appears to decrease a little,  $D$  increases and is prominent in the maximum phases, becoming lower in the minimum phases. In the ascending and descending transitions, the values are intermediate. This observation encourages us to perform a more thorough search for correlations with solar activity.

We can also obtain statistical information from Figs. 3a–b that can be used to distinguish fast wind from slow wind around the  $500 \text{ km s}^{-1}$  threshold. When comparing the values obtained for both complexity parameters between solar wind types, we observe that they are very close. However, there are differences and they are more appreciable in the  $D$  divergence means than for the  $\gamma$  exponent means. Even with the classification between solar wind types,  $\gamma$  almost behaves as a constant. On the other hand,  $D$  shows the same dependence on the solar phases for both slow and fast wind types, as in the black boxplots. We also note that  $D$  is always slightly higher for slow wind than for fast wind, except in ascending phases. The slow wind is highly variable, consistent with a higher level on  $D$ . If we plot just the mean values of Figs. 3a–b (diamond symbols), Fig. 3c verifies the anti-correlation between  $\gamma$  and  $D$ . The correlation coefficients between the complex parameters for the phase values only (i.e., if we focus on the triangles in Fig. 3c) are  $-0.992$  for unclassified solar wind (black triangles),  $-0.998$  for slow wind (blue triangles), and  $-0.882$  for fast wind (red triangles). Therefore, although the variations in  $\gamma$  are minor, the anti-correlation between the two measurements is clear, as can be seen in Fig. 3c. In addition, as seen in the same plot, the correlation between  $\gamma$  and  $D$  also depends on solar wind speed. The highest anti-correlation corresponds to slow solar wind magnetic fluctuations (blue symbols in Fig. 3c). More details about the values associated with the boxplots of Fig. 3 are given in Tables 1 and 2.

We also performed the analysis according to solar cycle phases. Figures 4 and 5 show  $\gamma$  and  $D$  as black curves, in contrast with  $S_n$  and  $v_p$  (in blue), respectively. In both figures, all curves have been smoothed by a yearly running average. The colored areas indicate the phases of the solar cycles and help us to distinguish the behavior of the curves as a function of solar activity.

First, relative to the sunspot number, in Fig. 4a we can see that  $\gamma$  exhibits an anti-correlation with sunspot number, especially within SC23. In general, the yearly smoothed curve presents values above  $\gamma_{\text{un}}$ , that is magnetic fluctuation time series correspond in general to correlated stochastic processes by definition. Also, the curve tends to decrease in correlation as it approaches the maximum (it approaches the  $\gamma_{\text{un}}$  limit). From Fig. 4b, we observe a particular match between the most prominent peaks of both curves in the maximum of SC23 (red circle on the left). In the maximum of SC24, the peak for the curve of  $D$  is in the gap between the double peaks of  $S_n$  (red circle on the right). Also, the baselines (inferior envelopes) follow each other, except for some delays, as in the ascending phase in SC24. At the minimum phases, the KLD values indicate reversible processes because the smoothed values of  $D$  are contained within the reversible range. Our results suggest a correlation between KLD and solar activity.

**Table 1.** Statistical information of the values obtained for the critical exponent.

		$\gamma$		Exponent			
	Period(s)	Mean	Median	Min.	25%	75%	Max.
Unclassified	Overall	0.505	0.512	0.198	0.482	0.537	0.644
	SC23	0.498	0.505	0.198	0.467	0.537	0.644
	SC24	0.513	0.517	0.306	0.494	0.537	0.604
	Minimum	0.524	0.525	0.414	0.501	0.549	0.617
	Ascending	0.498	0.510	0.306	0.475	0.533	0.604
	Maximum	0.488	0.500	0.198	0.451	0.525	0.614
	Descending	0.507	0.511	0.271	0.486	0.537	0.644
Slow wind	Overall	0.506	0.512	0.199	0.483	0.537	0.644
	SC23	0.497	0.506	0.199	0.466	0.537	0.644
	SC24	0.513	0.517	0.307	0.493	0.537	0.604
	Minimum	0.524	0.526	0.414	0.502	0.549	0.617
	Ascending	0.498	0.509	0.307	0.475	0.533	0.604
	Maximum	0.489	0.501	0.199	0.453	0.527	0.614
	Descending	0.508	0.512	0.271	0.490	0.539	0.644
Fast wind	Overall	0.504	0.510	0.198	0.480	0.537	0.640
	SC23	0.498	0.504	0.198	0.471	0.535	0.640
	SC24	0.511	0.516	0.306	0.495	0.537	0.601
	Minimum	0.522	0.523	0.427	0.497	0.551	0.615
	Ascending	0.500	0.512	0.306	0.474	0.533	0.601
	Maximum	0.481	0.495	0.198	0.442	0.520	0.596
	Descending	0.504	0.508	0.272	0.481	0.534	0.640

**Notes.** Values obtained from Fig. 3a for  $\gamma$ . These are the mean, median, minimum (Min.), maximum (Max.), and 25%–75% percentiles. The first panel covers the values for the entire solar wind, then the second and third panels cover the values for the solar wind classified between slow and fast wind. As in Fig. 3, the periods are for overall data, by cycle, and by total cycle-independent phases.

**Table 2.** Statistical information of the values obtained for the KLD.

		$D$		Divergence			
	Period(s)	Mean	Median	Min.	25%	75%	Max.
Unclassified	Overall	0.0111	0.0094	$1.7 \times 10^{-5}$	0.0062	0.0140	0.0458
	SC23	0.0121	0.0102	$2.7 \times 10^{-4}$	0.0062	0.0164	0.0457
	SC24	0.0104	0.0092	$1.7 \times 10^{-5}$	0.0066	0.0124	0.0439
	Minimum	0.0081	0.0074	$2.1 \times 10^{-4}$	0.0052	0.0104	0.0215
	Ascending	0.0129	0.0110	$1.7 \times 10^{-5}$	0.0073	0.0171	0.0458
	Maximum	0.0141	0.0124	$9.6 \times 10^{-4}$	0.0079	0.0179	0.0439
	Descending	0.0106	0.0095	$2.7 \times 10^{-4}$	0.0063	0.0130	0.0419
Slow wind	Overall	0.0112	0.0095	$6.7 \times 10^{-5}$	0.0064	0.0142	0.0447
	SC23	0.0125	0.0107	$3.0 \times 10^{-4}$	0.0065	0.0168	0.0447
	SC24	0.0105	0.0091	$1.7 \times 10^{-4}$	0.0065	0.0125	0.0439
	Minimum	0.0083	0.0077	$2.1 \times 10^{-4}$	0.0054	0.0108	0.0215
	Ascending	0.0127	0.0110	$1.7 \times 10^{-4}$	0.0073	0.0168	0.0447
	Maximum	0.0142	0.0124	$9.6 \times 10^{-4}$	0.0079	0.0182	0.0439
	Descending	0.0107	0.0094	$3.0 \times 10^{-4}$	0.0063	0.0130	0.0419
Fast wind	Overall	0.0105	0.0090	$1.7 \times 10^{-5}$	0.0059	0.0134	0.0458
	SC23	0.0111	0.0092	$2.7 \times 10^{-4}$	0.0055	0.0148	0.0458
	SC24	0.0100	0.0093	$1.7 \times 10^{-5}$	0.0069	0.0119	0.0364
	Minimum	0.0071	0.0066	$5.1 \times 10^{-4}$	0.0046	0.0086	0.0211
	Ascending	0.0136	0.0109	$1.7 \times 10^{-5}$	0.0071	0.0189	0.0458
	Maximum	0.0135	0.0121	$1.9 \times 10^{-3}$	0.0076	0.0171	0.0388
	Descending	0.0105	0.0096	$2.7 \times 10^{-4}$	0.0061	0.0132	0.0415

**Notes.** Values obtained from Fig. 3b for  $D$ . These are the mean, median, minimum (Min.), maximum (Max.), and 25%–75% percentiles. The first panel covers the values for the entire solar wind, then the second and third panels cover the values for the solar wind classified between slow and fast wind. As in Fig. 3, the periods are for overall data, by cycle, and by total cycle-independent phases.

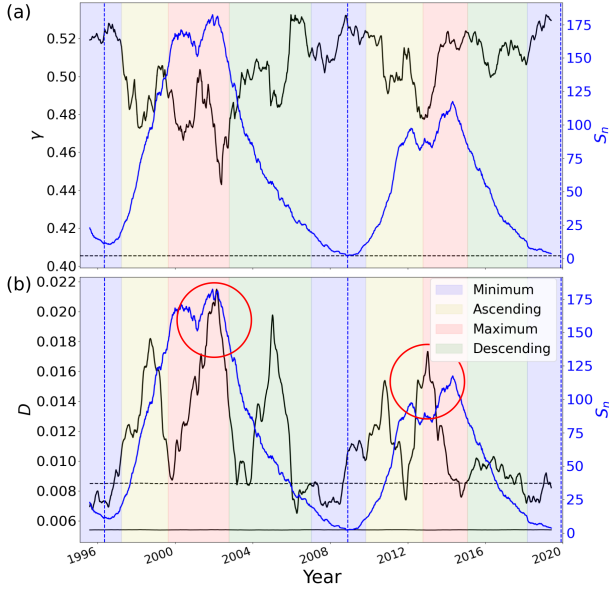


**Fig. 4.** Relations between solar activity and complexity parameters: all curves have been smoothed by a yearly running average of the values of  $\gamma$  and  $D$  (black curves) on the left axis and  $S_n$  (blue curves) on the right. Horizontal dashed black lines indicate the limit  $\gamma_{un}$  between chaotic and stochastic information in (a) and the upper half of the reversibility range over the continuous black line in (b). Vertical dashed blue lines delimit solar cycles 23 and 24. The colored blocks represent the phases of the solar cycles. The red circles mark the peaks of the  $D$  values at solar maxima. The time period is from 5 Aug 1995 to 29 May 2019.

Second, relative to the proton bulk speed, in Fig. 5a we can see that at the beginning of the SC23 (during the minimum and ascending phases),  $\gamma$  and  $v_p$  are correlated. However, in the following phases, this behavior tends to be reversed, as opposed to the behavior of the  $D$  curve. In Fig. 5b,  $D$  exhibits an anti-correlation with  $v_p$  from the beginning of the series, with a few partial exceptions (e.g., the second half of the ascending phase in SC23 and the descending phase in SC24). In most phases, both  $\gamma$  and  $D$  exhibit a certain anti-correlation with  $v_p$  in different manners.

The presence of clear correlations indicates the possible responsibility of a physical process relating to the quantities studied (this discussion is addressed in the last section). To explicitly follow correlations through these physical measures and the parameters of the complex network extracted from the magnetic time series of the solar wind, we tabulate correlation coefficients with their statistical significance: overall (from 5 Aug. 1995 to 29 May 2019), by cycle, and by phase in each cycle, in Tables 3 and 4. These tables provide the details of what we described from Figs. 4 and 5, with mostly robust statistical results.

## 5. Conclusions

Here we present a study of the information contained within a time series of solar wind magnetic fluctuations during solar cycles 23 and 24. To extract this information, we used the HVG algorithm, which establishes a geometric connection criterion based on the variability, sequence, and precedence of each data point of the series. With this technique, we derived degree distributions that provide information about time correlations present within the data. Further, we calculated two essential complexity parameters: the critical exponent,  $\gamma$ , and the Kullback–Leibler

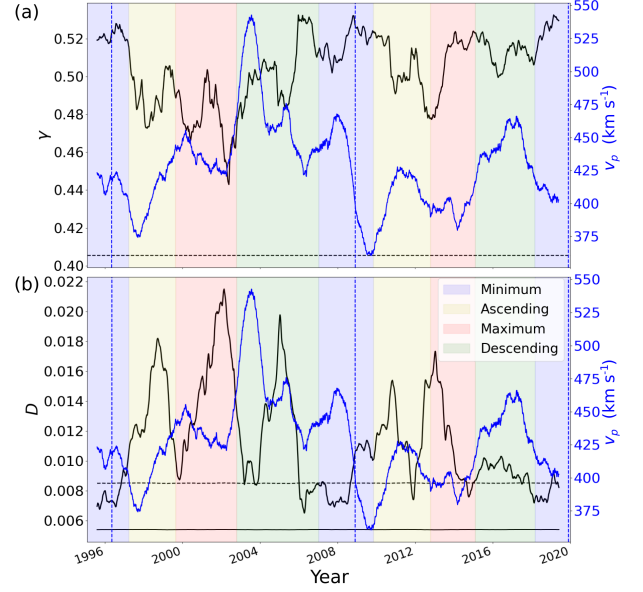


**Fig. 5.** Relations between solar wind speed and complexity parameters: All curves are smoothed by a yearly running average of the values of  $\gamma$  and  $D$  (black curves) on the left and  $v_p$  (blue curves) on the right. Horizontal dashed black lines indicate the limit  $\gamma_{un}$  between chaotic and stochastic information in (a) and the upper half of the reversibility range over the continuous black line in (b). Vertical dashed blue lines delimit solar cycles 23 and 24. The colored blocks represent the phases of the solar cycles. The time period covers from 5 Aug. 1995 to 29 May 2019.

**Table 3.** Pearson correlation coefficients and  $p$ -values between sunspot number and complexity parameters.

Period	$S_n$ vs. $\gamma$	$p$	$S_n$ vs. $D$	$p$
Overall	-0.72	<0.001	0.59	<0.001
SC23	-0.76	<0.001	0.62	<0.001
SC24	-0.44	<0.001	0.27	<0.001
min <sub>23</sub>	-0.88	<0.001	0.91	<0.001
asc <sub>23</sub>	0.13	<0.001	0.41	<0.001
max <sub>23</sub>	-0.25	<0.001	0.57	<0.001
des <sub>23</sub>	-0.68	<0.001	0.05	0.07
min <sub>23–24</sub>	-0.56	<0.001	-0.38	<0.001
asc <sub>24</sub>	-0.62	<0.001	-0.29	<0.001
max <sub>24</sub>	0.72	<0.001	-0.66	<0.001
des <sub>24</sub>	0.30	<0.001	0.59	<0.001
min <sub>24</sub>	-0.85	<0.001	-0.76	<0.001

**Notes.** Values obtained from the curves contrasted in Fig. 4. The first column indicates the period, where “min”, “asc”, “max”, and “des” denote the phase (minimum, ascending, maximum, descending) corresponding to the cycle indicated by its subindex. The second and fourth columns show the correlation coefficients between the  $S_n$  index with  $\gamma$ -exponent and  $D$ -divergence. The third and last columns display the  $p$ -values related to correlation coefficients of  $S_n$  with  $\gamma$  and  $D$ , respectively.

Divergence (KLD),  $D$ . The calculation of  $\gamma$  allows us to discriminate between correlated stochastic and uncorrelated chaotic series concerning the limit  $\gamma_{un} \approx 0.405$ . Moreover, as  $D$  moves away from  $D = 0$ , the physical mechanism that generated the time series moves away from reversibility. According to the shape of the degree distributions: if the  $\gamma$  value increases(decreases), it indicates short(long)-range

**Table 4.** Pearson correlation coefficients and  $p$ -values between proton bulk speed and complexity parameters.

Period	$v_p$ vs. $\gamma$	$p$	$v_p$ vs. $D$	$p$
Overall	-0.21	<0.001	-0.08	<0.001
SC23	-0.02	0.17	-0.20	<0.001
SC24	-0.11	<0.001	-0.33	<0.001
min <sub>23</sub>	0.87	<0.001	-0.97	<0.001
asc <sub>23</sub>	0.28	<0.001	0.39	<0.001
max <sub>23</sub>	-0.14	<0.001	-0.71	<0.001
des <sub>23</sub>	-0.60	<0.001	-0.05	0.06
min <sub>23-24</sub>	-0.67	<0.001	-0.95	<0.001
asc <sub>24</sub>	-0.46	<0.001	-0.21	<0.001
max <sub>24</sub>	0.10	<0.01	-0.03	0.44
des <sub>24</sub>	-0.01	0.76	0.24	<0.001
min <sub>24</sub>	-0.74	<0.001	-0.81	<0.001

**Notes.** Values obtained from the curves contrasted in Fig. 5. The first column indicates the period, where “min”, “asc”, “max” and “des” denote the phase (minimum, ascending, maximum, descending) corresponding to the cycle indicated by its subindex. The second and fourth columns show the correlation coefficients between the  $v_p$  solar wind speed with  $\gamma$ -exponent and  $D$ -divergence. The third and last columns display the  $p$ -values related to correlation coefficients of  $v_p$  with  $\gamma$  and  $D$ , respectively.

correlations, respectively; if the KLD value increases (decreases), the system is more(less) dissipative, respectively. By calculating the time evolution of both parameters, we can study the dissipative and stochastic features of the Sun by periods. We analyzed these values as a function of solar activity (in terms of solar cycles and cycle phases) and solar wind speed (slow and fast solar wind).

In terms of solar activity, our conclusions can be summarized as follows:

1. The HVG method is able to detect differences in intensity between SC23 and SC24 (this can be seen in Fig. 4). Previous studies show that SC24 had the lowest activity in terms of sunspots, even compared to the last five previous solar cycles (de Toma et al. 2010). From a general analysis of SC23 and SC24, we find that the  $\gamma$ -exponent reaches its minimum values in SC23 (see Fig. 3a), while the  $D$ -divergence is lower for SC24. Moreover, the behavior of the  $\gamma$  exponent suggests that, during both solar cycles, the magnetic fluctuations of the solar wind at 1 AU from the Sun are not chaotic and correspond to correlated stochastic time series. At large (or MHD) scales, the distributions of magnetic fluctuations show a rather Gaussian behavior, regardless of the type of wind. (Bruno & Carbone 2013). This can be observed in the nature of the turbulent energy transfer between different scales, which was recently modeled by Gallo-Méndez & Moya (2022) using the Langevin equation. Moreover, this behavior is also in agreement with the statistics of partial variance of increments (PVI) of the magnetic fluctuations presented by Greco et al. (2017), who obtained Gaussian PVI distributions at fluid scales. This Gaussian PDF of the PVI is associated with Brownian motion and Langevin processes in the solar wind, which correspond to a properly stochastic process. Also, our results show that  $D$  exhibits a correlation with solar activity, and in contrast, the  $\gamma$ -exponent appears to be anti-correlated with solar activity. Thus,  $\gamma$  and  $D$  are anti-correlated as verified in Fig. 3c. In summary, the solar wind plasma has turbulent struc-

tures, such that when the physical dissipative processes are less effective at large scales, they generate more correlated stochastic magnetic fluctuations. In any case, the intercorrelations vary throughout the solar cycle (see Table 3) because different solar magnetic configurations are possible in these cycles, even during very quiet periods, and the decrease in the sunspot index  $S_n$  may differ from the evolution of the interplanetary magnetic field (de Toma et al. 2010).

2. Exploring throughout solar phases, the minimum phases of each cycle coincide with the reversibility range of the KLD, and the maximum phases are recognized as larger values of KLD. As  $D$  is a ratio between forwards and backwards in time connections, when  $D$  increases, this indicates that the distribution of relative magnitudes in the data is different between their forward and backward visibility within the network, which makes the time series more irreversible. The generation and transport of magnetic fluctuations in the turbulent solar wind correspond to a memoryless process, that is, a Markovian process (Strumik & Macek 2008). As greater irreversibility (consistent with Markovian processes) is observed in solar maxima, large-scale instabilities, which are understood to be one the most important physical mechanisms responsible for the generation of turbulence, are likely to be dominating in these periods. Thus, at solar minima, the fluctuations are less complex and less turbulent. In addition, the  $\gamma$  value seems to increase with decreasing magnetic activity in the Sun, that is, when fewer sunspots are seen in the photosphere. This calculation means that the distribution of connections is more concentrated, which means a few nodes share all the connections. In summary, and as detailed in Tables 1 and 2, this study reveals that, in terms of solar phases,  $\gamma_{\min} > \gamma_{\text{des}} > \gamma_{\text{asc}} > \gamma_{\text{max}}$ , and  $D_{\min} < D_{\text{des}} < D_{\text{asc}} < D_{\text{max}}$ . Thus, the complexity parameters calculated here are consistent with the turbulent nature of the solar wind and its generation at the Sun.
3. With the chosen timescale to calculate the complexity parameters in the study and the yearly smoothing applied, we observed that each phase contains its own peak in the value of  $D$ . This relation could provide relevant and complementary information to the sunspot number measurement and possible forecasts of the solar cycle. Namely, if a peak in  $D$  has occurred, it is likely that the phase is coming to its end. Moreover, the fact that the minimum phases are captured by the reversibility range suggests that the solar wind has memory at those times, which is related to non-Markovian processes consistent with a less complex (and more dipolar) interplanetary magnetic field generated by the quiet Sun (McComas et al. 2008). Such behavior could robustly contribute to the predictability of the onset of a solar cycle. Thus, the KLD can be useful as a statistical measure to compare behaviors in the future with behaviors in the past. However, further supporting information would be needed to corroborate this idea. Regarding solar wind speed, our findings are as follows:
4. Given the classification between fast and slow wind according to the speed, the exponent  $\gamma$  behaves uniformly. Its variations for fast and slow solar wind concerning the general (unclassified) behavior are not at all evident (see Fig. 3a). This conclusion is in agreement with the results of Sorriso-Valvo et al. (1999), who indicated that the intermittency (interpreted as the result of the multifractal properties of the turbulent cascade and due to the contribution from non-Alfvénic structures (Wawrzaszek et al. 2019) of the magnetic field intensity was similar for the slow and

fast wind. On the other hand, directed degree distributions can clearly be used to distinguish the type of solar wind through the KLD. From Table 2, the slow wind, which is more variable, is precisely the type of wind that achieves the highest values in the  $D$ -divergence; except in the ascending phase, where only the median (and not the mean) corroborates this, as shown in Fig. 3b. Although the fast wind has generally been observed to be less intermittent than the slow wind (Marsch & Liu 1993), as the fast wind is more Alfvénic than the slow wind, Wawrzaszek et al. (2019), surprisingly, detected that the magnetic field turbulence of the slow solar wind was less intermittent at the SC23 maximum. Our results do not reveal any peculiarity in the SC23 maximum that could support the idea of a new type of slow Alfvénic wind. However, in the ascending phases, we find the slow wind to be less irreversible. Perhaps, the method we present here could detect the presence of Alfvénic slow wind (with some characteristics common to the fast wind) before the maximum phases.

5. In Fig. 5 the critical exponent and KLD have a dynamic intercorrelation throughout the cycles. However, in Table 4,  $\gamma$  does not tend to exhibit significant linearity with solar wind speed. Figure 5b shows an anti-correlation between the  $D$ -divergence and the solar wind proton bulk speed. This anti-correlation, according to the numbers in Table 4, is most significant at the minimum of each cycle, which could also allow us to estimate the start of a cycle combined with the fact that, in the minimum phase,  $D$  allows a clearer disentanglement of the slow solar wind from the fast solar wind.
6. Distinguishing fast solar wind from slow wind using the HVG technique seems more useful during solar minimum than other phases. As mentioned in Conclusion #3, this ability is likely because the minimum phase is when the Sun's magnetic field is more dipolar, and the solar wind structure is less complex. On the other hand, at the maximum phase, the solar wind is a particularly nonlinear combination of various solar wind types. McComas et al. (2008) state that the heliospheric current sheet is complex and dynamic in itself, but around the maximum phase, highly variable solar wind fluxes are observed at all heliolatitudes, which change the configuration of the current-sheet structure as a whole. Our results indicate that the slow solar wind is more dissipative than the fast wind in terms of magnetic fluctuations in most phases of the cycle, which is consistent with the evolving and fully developed turbulence of the fast and slow solar wind, respectively (see e.g., D'Amicis et al. 2018, and references therein). Further improvement to the solar wind classification procedure by considering parameters in addition to speed (Wawrzaszek et al. 2019) will allow more conclusive verification of this analysis.

In summary, our results suggest that the intercorrelations of the complexity parameters with the sunspot number index are persistent in time. These intercorrelations can be seen over extended periods, in this case from 1995 to 2019, or by solar cycle, but in shorter periods they are also preserved. In contrast, the intercorrelations we find with the proton bulk speed are short-range and are only best analyzed on shorter timescales, such as solar phases. Both  $\gamma$  and  $D$  show more considerable and statistically significant intercorrelations with sunspot number than solar wind speed. According to the observational data input and the degree distributions output through the HVG method, our results are consistent with the complex nature of solar wind turbulence at 1 AU and its relation with the complexities of the solar cycle.

We expect our results to be relevant for the understanding of the physics of the solar wind. We hope that this type of analysis, used in complex networks and systems science, can contribute to heliophysics through tools that allow data to be analyzed in new ways, even when information is limited. Our analysis could be relevant for the complementarity of physical variables that can be measured thanks to the progress of space exploration, but also as an approach to characterize stellar activity where direct in situ measurements of stellar winds are unavailable.

*Acknowledgements.* We thank the Wind mission, NASA CDAWeb, and World Data Center SILSO. ANID Chile supported this work through Fondecyt grant number 1191351.

## References

- Acosta-Tripailao, B., Pastén, D., & Moya, P. S. 2019, *Proc. Int. Astron. Union*, **15**, 363
- Acosta-Tripailao, B., Pastén, D., & Moya, P. S. 2021, *Entropy*, **23**, 470
- Acosta-Tripailao, B., Max-Moerbeck, W., Pastén, D., & Moya, P. S. 2022, *Entropy*, **24**, 1063
- Albert, R., & Barabási, A.-L. 2002, *Rev. Mod. Phys.*, **74**, 47
- Alberti, T., Consolini, G., Carbone, V., et al. 2019, *Entropy*, **21**, 320
- Balogh, A., & Lanzerotti, L. J. 2008, *The Heliosphere through the Solar Activity Cycle* (Berlin: Springer), 1
- Borovsky, J. E. 2021, *Front. Astron. Space Sci.*, **200**
- Bruno, R., & Carbone, V. 2013, *Liv. Rev. Sol. Phys.*, **10**, 1
- Chhiber, R., Matthaeus, W. H., Bowen, T. A., & Bale, S. D. 2021, *ApJ*, **911**, L7
- Cover, T. M., & Thomas, J. A. 2006, *Internet Access* (Wiley-Interscience)
- D'Amicis, R., Matteini, L., & Bruno, R. 2018, *MNRAS*, **483**, 4665
- de Toma, G., Gibson, S., Emery, B., & Arge, C. 2010, in *SOHO-23: Understanding a Peculiar Solar Minimum*, 428, 217
- Gallo-Méndez, I., & Moya, P. S. 2022, *Sci. Rep.*, **12**, 1
- Greco, A., Matthaeus, W., Perri, S., et al. 2017, *Space Sci. Rev.*, **214**, 1
- Gupta, K., Prasad, A., Saikia, E., & Singh, H. P. 2008, *Planet. Space Sci.*, **56**, 530
- Kilpua, E., Olsper, N., Grigorievskiy, A., et al. 2015, *ApJ*, **806**, 272
- Lacasa, L., & Toral, R. 2010, *Phys. Rev. E*, **82**, 30001
- Lacasa, L., Luque, B., Ballesteros, F., Luque, J., & Nuno, J. C. 2008, *Proc. Natl. Acad. Sci.*, **105**, 4972
- Lacasa, L., Luque, B., Luque, J., & Nuno, J. C. 2009, *Europhys. Lett.*, **86**, 30001
- Lacasa, L., Nunez, A., Roldán, É., Parrondo, J. M., & Luque, B. 2012, *Eur. Phys. J. B*, **85**, 1
- Lepping, R., Acuña, M., Burlaga, L., et al. 1995, *Space Sci. Rev.*, **71**, 207
- Luque, B., Lacasa, L., Ballesteros, F., & Luque, J. 2009, *Phys. Rev. E*, **80**, 046103
- Macek, W. M., & Redaelli, S. 2001, *AdSpR*, **28**, 775
- Marsch, E., & Liu, S. 1993, *Ann. Geophys.*, **11**, 227
- Marsch, E., & Tu, C. 1994, *Ann. Geophys.*, **12**, 1127
- McComas, D., Elliott, H., Schwadron, N., et al. 2003, *Geophys. Res. Lett.*, **30**
- McComas, D., Ebert, R., Elliott, H., et al. 2008, *Geophys. Res. Lett.*, **35**
- Mohammadi, Z., Alipour, N., Safari, H., & Zamani, F. 2021, *J. Geophys. Res. Space Phys.*, **126**, e2020JA028868
- Ogilvie, K., Chornay, D., Fritzenreiter, R., et al. 1995, *Space Sci. Rev.*, **71**, 55
- Podesta, J., Roberts, D., & Goldstein, M. 2007, *ApJ*, **664**, 543
- Reda, R., Giovannelli, L., Alberti, T., et al. 2021, *IL NUOVO CIMENTO*, **100**, 44
- Redaelli, S., & Macek, W. M. 2001, *Planet. Space Sci.*, **49**, 1211
- Reyes, P. I., Pinto, & V. A., Moya, P. S. 2021, *Space Weather*, **19**, e2021SW002766
- Roberts, D. A. 2007, in *AGU Fall Meeting Abstracts*, 2007, SH31B-06
- Roberts, O. W., Thwaites, J., Sorriso-Valvo, L., Nakamura, R., & Vörös, Z. 2020, *Front. Phys.*, **8**, 584063
- Roldán, É., & Parrondo, J. M. R. 2012, *Phys. Rev. E*, **85**
- Shepherd, S. J., Zharkov, S. I., & Zharkova, V. V. 2014, *ApJ*, **795**, 46
- Sorriso-Valvo, L., Carbone, V., Veltri, P., Consolini, G., & Bruno, R. 1999, *Geophys. Res. Lett.*, **26**, 1801
- Sorriso-Valvo, L., Carbone, V., Giuliani, P., et al. 2001, *Planet. Space Sci.*, **49**, 1193
- Sorriso-Valvo, L., Carbone, F., Leonardis, E., et al. 2017, *AdSpR*, **59**, 1642
- Strumik, M., & Macek, W. M. 2008, *Phys. Rev. E*, **78**, 026414
- Suyal, V., Prasad, A., & Singh, H. P. 2012, *Sol. Phys.*, **276**, 407
- Suyal, V., Prasad, A., & Singh, H. P. 2014, *Sol. Phys.*, **289**, 379
- Wawrzaszek, A., Echim, M., & Bruno, R. 2019, *ApJ*, **876**, 153